# Differences in cell shape, motility, and growth reflect chromosomal number variations that can be visualized with live-cell ChReporters

Michael P. Tobin®†, Charlotte R. Pfeifer†, Peter Kuangzheng Zhu, Brandon H. Hayes, Mai Wang, Manasvita Vashisth, Yuntao Xia, Steven H. Phan, Susanna A. Belt, Jerome Irianto®, and Dennis E. Discher\*

Mol. Cell Biophysics Lab, University of Pennsylvania, Philadelphia, PA 19104

ABSTRACT Chromosome numbers often change dynamically in tumors and cultured cells, which complicates therapy as well as understanding genotype-mechanotype relationships. Here we use a live-cell "ChReporter" method to identify cells with a single chromosomal loss in efforts to better understand differences in cell shape, motility, and growth. We focus on a standard cancer line and first show clonal populations that retain the ChReporter exhibit large differences in cell and nuclear morphology as well as motility. Phenotype metrics follow simple rules, including migratory persistence scaling with speed, and cytoskeletal differences are evident from drug responses, imaging, and single-cell RNA sequencing. However, mechanotype-genotype relationships between fluorescent ChReporter-positive clones proved complex and motivated comparisons of clones that differ only in loss or retention of a Chromosome-5 ChReporter. When lost, fluorescence-null cells show low expression of Chromosome-5 genes, including a key tumor suppressor APC that regulates microtubules and proliferation. Colonies are compact, nuclei are rounded, and cells proliferate more, with drug results implicating APC, and patient survival data indicating an association in multiple tumor-types. Visual identification of genotype with ChReporters can thus help clarify mechanotype and mechano-evolution.

# **Monitoring Editor**

Valerie Marie Weaver University of California, San Francisco

Received: Jun 5, 2023 Revised: Sep 15, 2023 Accepted: Oct 10, 2023



### SIGNIFICANCE STATEMENT

- Cultured cells, tumors, and early embryos generally have abnormal numbers of chromosomes that
  also differ dynamically between cells, but impact on mechanotype is understudied.
- Fluorescence-based ChReporters enable live-cell visualization of chromosome number differences, which can help relate to single cell mechanotypes.
- Morphology, motility, and growth sometimes relate to such visible genotype differences, which helps to clarify processes in mechano-evolution.

This article was published online ahead of print in MBoC in Press (http://www.molbiolcell.org/cgi/doi/10.1091/mbc.E23-06-0207).

 $\ensuremath{^{\dagger}} \text{These}$  authors contributed equally to this work and should be regarded as the co-first authors.

\*Address correspondence to: Dennis E. Discher (discher@seas.upenn.edu).

Abbreviations used: APC, adenomatous polyposis coli; Chr, chromosome; CNV, copy number variation; Lat, Latrunculin; LMNB1, Lamin-B1; LOH, loss of heterozygosity; MTs, microtubules; Noc, Nocodazole; RFP, red fluorescent protein; TCGA, The Cancer Genome Atlas.

© 2023 Tobin et al. This article is distributed by The American Society for Cell Biology under license from the author(s). Two months after publication it is available to the public under an Attribution–Noncommercial-Share Alike 4.0 International Creative Commons License (http://creativecommons.org/licenses/by-nc-sa/4.0). "ASCB®," "The American Society for Cell Biology®," and "Molecular Biology of the Cell®" are registered trademarks of The American Society for Cell Biology.

### INTRODUCTION

The DNA sequence in a viable cell can change as a result of physical stressors that range from radiation to mechanical strain (Hayes et al., 2023). However, understanding any subsequent effects on a cell's phenotype – particularly its mechanotype – requires clear measures of the genotype of that individual living cell. In most cell lines and nearly all solid tumors, chromosome (Chr) losses and gains are typical and variable, altering the DNA from the 46 Chrs of a normal diploid cell (Table 1; Supplemental Figure S1A). This aneuploidy or copy number variation (CNV) is generally not static but ongoing (Holland and Cleveland, 2009), so that chromosomal differences between cells complicates single cell studies – including mechanobiology

Human Cell Line	Modal # of Chrs	Heterogeneity (% cells different)	Heterogeneity (Range, # of Chrs)
MCF7 (Breast Cancer)	82	-	66–87 (26% of mode)
MDA-MB231 (Breast Cancer)	64	_	52–68 (25% of mode)
A549 (LUAD)	66	76%	_
HepG2 (Liver cancer)	55	_	50–60 (20% of mode)
HEK293 (Normal Fetal Kidney)	64	70%	_
U-87 (Glioma)	44	52%	-
THP-1 (Leukemia)	~48 (consensus clone)	27%	47–49 (2% of mode) **

Data from American Type Culture Collection, ATCC (see Methods), except THP-1 (Wang et al., 2023).

TABLE 1: Commonly used cell lines typically show high genotypic variation.

studies. Heterogeneity also frustrates cancer therapies such as targeted immunotherapies (Davoli et al., 2013). Loss of a Chr leads on average to proportional decreases in transcripts and proteins expressed from the affected Chr, and a gain has the opposite effect (Pavelka et al., 2010; Torres et al., 2010; Stingele et al., 2012). In yeast, disproportionate protein levels from aneuploid states alter the free versus bound levels in the normal stoichiometry of interacting proteins, affecting cell osmolarity and a cell's mechanical stress state (Tsai et al., 2019). Visualizing a living cell's genotype should thus help clarify mechanotypic variation.

Cancer geneticists often assume that loss (or gain) of a specific Chr leads to a phenotype that mainly reflects the loss (or gain) of a "key" tumor suppressor gene (or cancer-driving oncogene) on that particular Chr (Davoli et al., 2013). Major deficiencies or defects in just a few such "key" genes seems sufficient to drive cancer and thus cannot be compensated by other genes (Martincorena et al., 2017). Of relevance to studies here is the loss of Chr-5 that decreases expression of all Chr-5 genes including the tumor suppressor Adenomatous polyposis coli (APC). We hypothesized that mechanotypic signatures of morphology, motility, and growth can relate to dominating differences in such a specific Chr loss particularly when we visualize Chr differences between cells.

To address our hypothesis, we developed a general "ChReporter" method that allows us to see a specific Chr loss in a living cell (Hayes et al., 2023). As one particular example, the constitutive gene Lamin-B1 on Chr-5 was gene-edited as a monoallelic RFP or GFP fusion such that visible loss of the fluorescent signal signifies loss of one copy of Chr-5. Detecting an increase in RFP signal can in principle be used to detect a Chr gain, but levels of Lamin-B1 happen to increase about two-fold from G1 to G2/M (Hayes et al., 2023) whereas complete loss of signal is more obvious. In standard cultures of many cell lines, micronuclei are frequently seen and contain chromosomal DNA (Figure 1A image, arrow) before loss or gain of a Chr in daughter cells of subsequent cell generations. Indeed, we have recently shown that rare RFP-negative cells emerging from pure RFP-positive cells (Figure 1A) not only reflect loss of one allele of Chr-5 but also relate to abnormal mitosis on a range of substrate stiffnesses; these included collagen-coated soft gels on which cells exhibited more frequent mitotic errors and significantly higher Chr-5 loss than cells on plastic despite reduced proliferation (Hayes et al., 2023). Genetic methods applied to lysed or fixed dead cells can confirm presumed changes in Chr number (e.g., Supplemental Figure S1B, i), but such methods lack sensitivity to rare cells and lack spatiotemporal information. Simple visualization of CNV within live cells by ChReporters should thus accelerate insight and add confidence in studies despite ongoing instability and genetic diversification of the cells being studied (Supplemental Figure S1B, ii).

Our ChReporter method has been used to study multiple Chrs in normal diploid iPS cells and various cancer-cell lines (Hayes et al., 2023), including the A549 cells derived long ago from a patient with lung adenocarcinoma (LUAD; Giard et al., 1973). The A549 line is widely used to model normal lung epithelium (Foster et al., 1998; Carterson et al., 2005), but patients with such solid tumors are known to possess many CNV's even though loss or gain of whole Chr-5 in patients is rare (Supplemental Figure S2A). Although this observation suggests little advantage (i.e., neutral drift) for losing Chr-5 in terms of net growth and invasiveness of LUAD, rare Chr loss plus various epigenetic and mutational mechanisms can result in low APC levels that seem prognostic of poor survival in lung cancer (Supplemental Figure S2B, i) in addition to the well-appreciated effect in colorectal cancer even with immunotherapy (He et al., 1998; Hankey et al., 2018). We therefore sought to clarify genotypemechanotype relationships in vitro with A549 cells using our Chr-5 ChReporter and a progressive focus on the APC pathway.

### **RESULTS**

To illustrate mechanotype-genotype complexity, we focus first on four A549 clones that are all RFP-positive. Standard single cell expansion of clones P1-P4 began from a mixed population of RFPpositive cells and rare RFP-negative cells, with the latter being the source of N1-N4 clones studied later (Figure 1A). While A549 cells undergo frequent changes to aneuploid states with high genetic variation (Table 1; Supplemental Figure S1, A and B), many isolated clones grow similarly with no major advantage from chromosomal selection (Supplemental Figure S1B, ii). Imaging P1 cells reveals a more rounded shape than P2-P4 clones, with morphological parameters for aspect ratio and circularity following a simple ellipse model prediction (Figure 1B-i; Xia et al., 2018). Depolymerization of MTs with Nocodazole drives cell rounding (Chang et al., 2008), and Nocodazole treatment of the highly elongated P3 cells phenocopied the rounded P1 cells (Figure 1B, i, inset). Depolymerization of F-actin with Latrunculin-A should also favor cell rounding (Spector et al., 1989), and although the effect is somewhat less than with Nocodazole, both drug results conform to the ellipse model. RFP-Lamin-B1 images also show more rounded P1 nuclei (Figure 1B, ii). Nuclear shape trends track cell shapes but span a narrower range likely because nuclei are less deformable (Buxboim et al., 2017).

Defects in major cytoskeletal proteins seemed likely to underlie the distinctive morphology of P1 cells and suggested defects in other cytoskeletal-driven processes such as motility. Live imaging of sparsely plated clones was thus used to measure cell speed and persistence, showing P1 cells migrate far slower and with less persistence than P2–P4 cells (Figure 1C). P4 cells are intermediate, consistent with an intermediate shape of the nucleus if not the cell.

FIGURE 1: Clonal populations exhibit distinct morphology and motility mechanotypes. (A) Sorted RFP-pos A549s in standard culture lead to rare RFP-neg cells that indicate Chr-5 loss (Supplemental Figure S1B). A micronucleus illustrates ongoing chromosomal instability. Four RFP-pos and RFP-neg cells were clonally expanded for studies of mechanotype and genotype. (B; i) P1 cells are round in both sparse and crowded cultures. Inset: P3 cells phenocopy P1 when MTs or F-actin are disrupted using Nocodazole (Noc.) or Latrunculin-A (Lat). (Mean and SEM; >100 cells per condition; \*p < 0.001). (ii) Nuclei align with cell morphologies. (Mean and SEM; >185 cells per condition; \*p < 0.001). (C) Live-imaging of sparse RFP-pos clone cultures for 6 h reveals differences in cell motility and shows persistence scales with migration speed. Each colored trajectory represents a cell. Inset: P1 cells are again phenocopied by P3 cells treated with Noc. or Lat. (Mean and SEM; >100 cells per condition; \*p < 0.001). (D) Cytoskeletal filaments dictate morphological and motility responses in cells. Depolymerization of long structural MTs (with Noc.) results in significant cell rounding. In highly elongated cells, such as P3 cells, the MT organizing center (MTOC) is well-defined near the nucleus. In comparison, migratory persistence is most disturbed after F-actin inhibition. E; i) scRNA-seq of the four RFP-pos clones reveals low beta tubulin and beta actin in P1 (\*p < 0.05; Wilcoxon rank sum with Bonferroni correction). (ii) Average results confirms P1 cells have lower beta tubulin and beta actin, although both are highly expressed. Inset: Four gene categories that are most enriched (red) or deficient (blue) in P1 cells relative to other clones show cytoskeleton genes are most deficient. (iii) Across all Chrs, Chr 7 contains the largest increase in P1 genes relative to other clones; however, Chr 1 and 17 also have many distinctly expressed genes. (iv) Chr distribution of all genes that show >1.28-fold change in all RFP-pos cells versus all RFP-neg cells (red bars) or >1.28-fold change in RFP-neg versus RFP-pos (white bars). The ChReporter system enables more precise study of gene downregulation of Chr 5. Dashed line is mean average and gray box is SD.

0.0

1e-4

0.01

Mean reads of P1

lean

P4 P3 P2 P1

See.

P3 P2 P1

P4 P3 P2 P1

RFP-pos

RFP-neg

10

10 Chr# 15

100

Regardless, the ~10-fold range in persistence helps convince that clone migration fits a power law:

Persistence 
$$\sim \lceil \text{Speed} \rceil^2$$
 (1)

Such a power law seems new for the field, especially when comparing clones from the same cancer line of common genetic origin and similar epigenetics, which is relevant to tumor processes such as Epithelial-to-Mesenchymal transitions (EMT). The scaling exponent of about 2 also aligns with our analysis of past studies (Supplemental Figure S3A; *Materials & Methods*). Furthermore, highly motile P3 cells treated with Nocodazole and Latrunculin-A phenocopied the low motility of P1 cells and scaled per Eq.1 (Figure 1C inset). These mechanotype results suggest P1 cells are defective in MT, actin, and/or related cytoskeletal factors (Figure 1D).

Given the overall hypothesis that differences in mechanotype properties relate to differences in specific Chr losses or gains, we explored whether apparent cytoskeletal deficiencies in P1 cells result from gene expression decreases related to Chr loss. Single cell RNA-seq (scRNA-seq) was thus performed on the various clones, showing that major cytoskeletal genes such as beta tubulin (TUBB) and beta actin (ACTB) were highly downregulated in P1's whereas other related genes such as CDH2 show no change (Figure 1E, i). Average sc-RNAseq show reduced expression of P1's TUBB and ACTB even though overall RNA levels remain high (Figure 1E, ii). Overall, cytoskeleton genes are among the most downregulated genes, confirming phenotypic observations of P1's compared with other P-clones (Figure 1E, ii, inset). Further, immunostaining for MT's reveals MT organizing centers (MTOC) are suppressed in P1 versus P3 cells, providing insight into impaired MT functionality in P1 cells (Supplemental Figure S3B). Also, the essential role of MT's in mitosis is well-illustrated by Nocodazole effects (De Brabander et al., 1976); defective MT's in P1 cells should and do suppress proliferation (Supplemental Figure S3, C and D).

Upon deeper analysis of distinct P1 genes per Chr, several Chr's show large differences for P1 versus P2-4, with Chr-7 showing the biggest increases (Figure 1E, iii). Importantly, Chr-5 shows no significant changes, consistent with our ChReporter method. However, other disparities (e.g., Chr's 1 and 17) confound deeper understanding of P1's specific mechanotype, which illustrates the complexity of untangling genotype—mechanotype relationships. Potentially, livecell genetic approaches such as the ChReporter can begin to help, and comparing RFP-pos versus RFP-neg indeed shows a clearer genotype versus fluorescence phenotype difference, consistent with the expected Chr-5 difference (Figure 1E, iv). This supports our visual ChReporter approach and motivates study of gene dosage effects between various P and N clones.

To pinpoint differences in genomic DNA rather than merely inferring differences from RNA, we analyzed Single Nucleotide Polymorphism (SNP)-array (SNPa) data for DNA isolated from each of the eight clones. Multiple Chr losses and gains are indeed clear relative to the P3 population (Figure 2A), with Chr-5 lost in all N clones. N2-4 clones descend directly from P3 Chr-5 loss, whereas N1's seem to derive differently (Figure 2A, bot) and indicate diverse processes of loss or gain from genome instability (e.g., Figure 1A, inset). P1 shows Chr-7 gain, as inferred by scRNA-seq (Figure 1E, i–iii) as made clear in standard UMAP projections (Figure 2B). The P versus N difference arising from Chr-5 loss in the UMAP is also clear in a heatmap of each N when rescaled by the average of all P (Figure 2C, i).

Rather than comparing many different clones in terms of mechanotype that will emerge from the evolving genotype heterogeneity typical of cancer and cell lines (Supplemental Figure S1A), we

instead focus on N3 and P3 clones with clear genetic differences only on Chr-5 (Figure 2A). Genetic heterogeneity nonetheless emerges in these based on the observation that ChReporters can be lost under control conditions to a ~0.5% level within days (Hayes et al., 2023); however such variance is more random and unbiased than the visible ChReporter difference that remains between these two populations after weeks of passaging (Supplemental Figure S3E). Furthermore, if any P3 cells lose this same Chr in the course of study (per Figure 1A), then the cells and colonies become RFP-neg and can be ignored. In the future, use of multiple ChReporters can generalize the approach. Regardless, N3 cells show the expected gene dosage downregulation of most Chr-5 genes, including Lamin-B1, compared with P3 cells (Figure 2, C ii, and D). Downregulation includes the APC tumor suppressor gene, which is notable because Chr loss is frequently associated by cancer geneticists to loss of such key tumor suppressor gene(s) that then drives the cancer (Davoli et al., 2013). Indeed, based on prior pancancer analyses, APC is by many orders of magnitude the highest ranked of just eight significant tumor suppressor genes on Chr-5 (Figure 2E; Supplemental Table S1). Reduced expression of the APC gene can affect its functionality, altering its ability to act as a WNT-signaling pathway antagonist, stabilize MTs, or permit cell motility (Faux et al., 2004; Wen et al., 2004; Schneikert and Behrens, 2007). Given observed Chr-5 copy number differences in living N3 and P3 cells, we hypothesize that mechanotype-related properties including aspects of morphology, motility, and proliferation can relate for N3 versus P3 to differences in APC levels despite the overall aneuploid background of the cells. Although variation of Chr-5 in lung cancer patients is relatively rare (Supplemental Figure S2), loss of a tumor suppressor can increase invasiveness and proliferation (Davoli et al., 2013) and might also affect other hallmarks of cancer (Hanahan and Weinberg, 2011).

To begin to compare P3 and N3 mechanotypes, we imaged sparse cultures, which contained small proliferating clusters. Morphological differences were significant, with N3 colonies showing higher circularity or compactness versus P3 colonies (Figure 3A). Cells that were isolated and well-separated from clusters displayed a typical migratory mechanotype but were several-fold less frequent for N3 cells, yielding an anticorrelation between cluster circularity and lone migratory cells (Figure 3A, plot). Because cell–cell adhesions as represented by junctional  $\beta$ -catenin intensities were statistically the same for N3 and P3 (shown below), it is plausible that the migration is suppressed for N3 cells. These results thus raised the possibility of a "go or grow" competition (Giese et al., 1996), which proposes that cells which migrate fast and far do not divide very frequently, although the idea remains debated (Zheng et al., 2009; Garay et al., 2013; Pfeifer et al., 2018).

To examine migration coupled to proliferation, cells were densely seeded on Top of transwell filters with 8-µm pores. These pores were used previously to reveal "go and grow" in 3D without the complications of nuclear rupture and DNA damage that are caused by smaller pores (Irianto et al., 2017). Given that APC is a tumor suppressor and the low frequency of cluster-isolated motile N3 cells (Figure 3A), one prediction is that N3 cells migrate more slowly from the contact-inhibited transwell Top to the Bottom but reenter the cell cycle and grow more quickly on Bottom during the 1-d assay. Such offsetting processes can explain the statistically similar fractions of cells that have localized to Bottom for N3 and P3 (Figure 3B, i). Further, consistent with the prediction, N3 cells showed two-fold greater mitotic cell counts and EdU incorporation, indicating DNA replication and enhanced reentry into cell cycle following migration from the contact-inhibited Top (Figure 3B, ii).

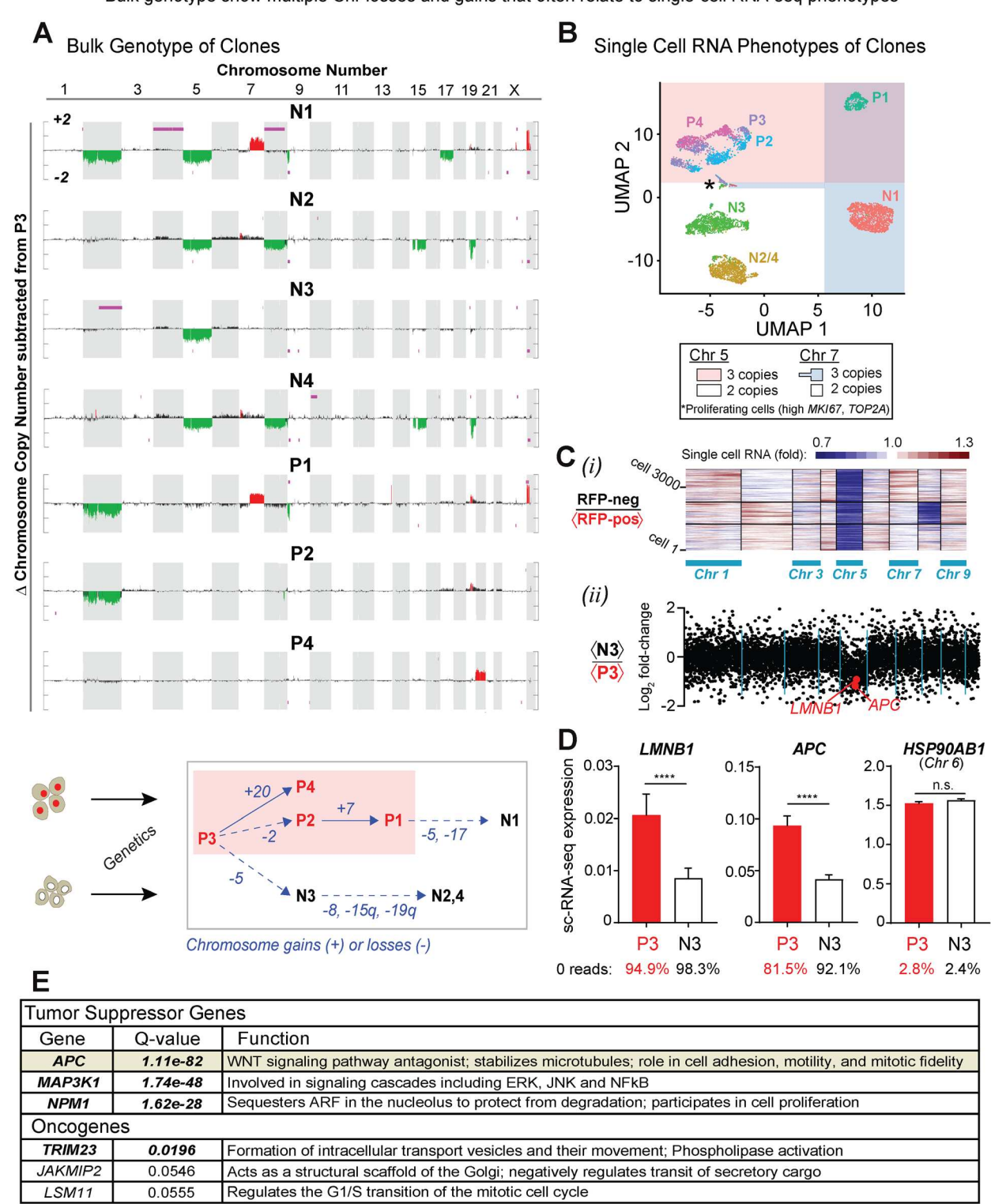
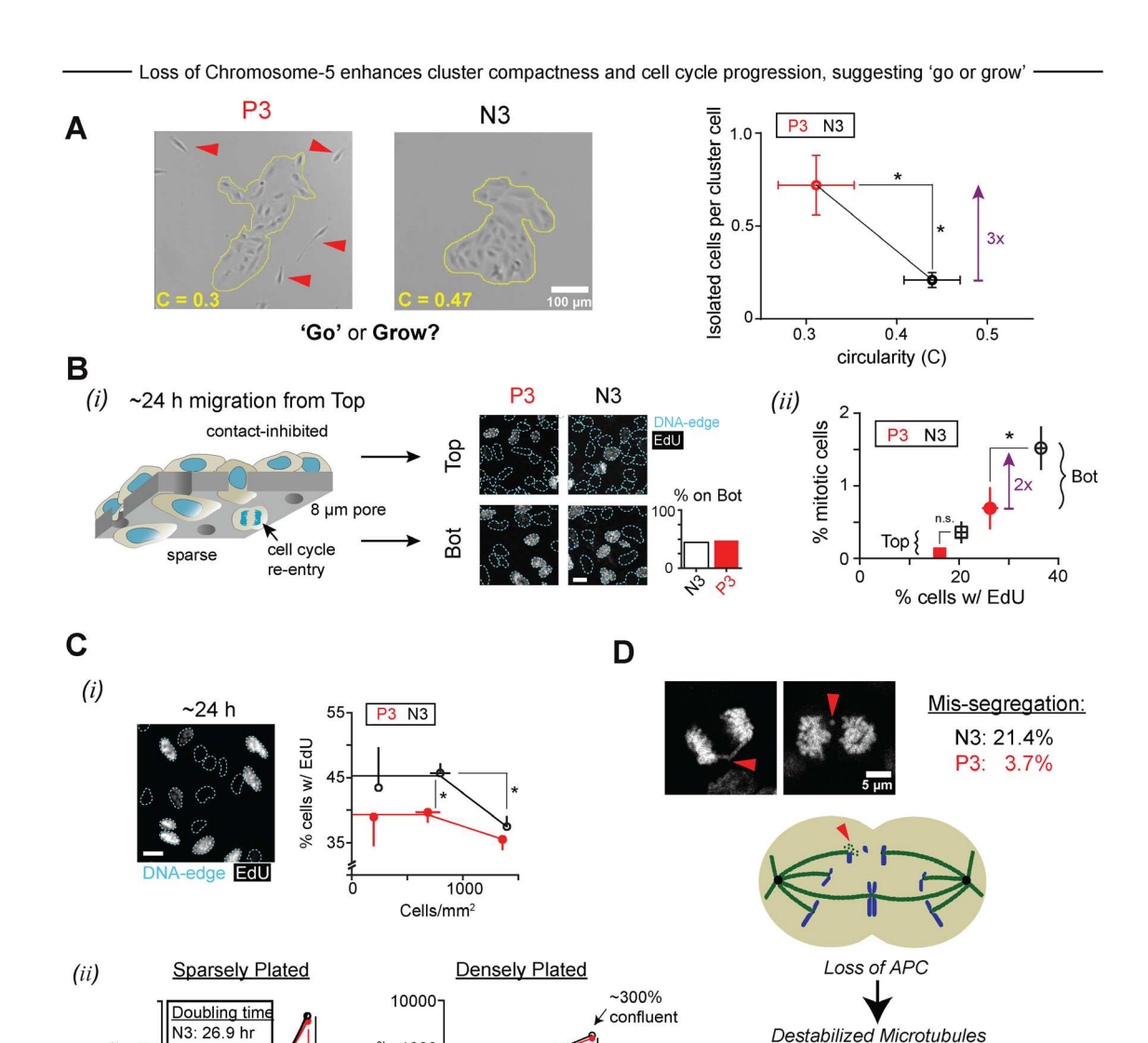


FIGURE 2: Bulk genotypes show multiple Chr losses and gains that often relate to single-cell RNA-seq phenotypes. (A) Top: SNP arrays on bulk clones compared with parental P3. RFP-neg clones exhibit a loss of Chr 5. Bottom: Lineage map summary (blue). (B) Single-cell RNA-seq reveals Chr copy dominated differences; UMAP1 correlates with Chr 7 differences and UMAP2 with Chr 5 differences. (C) Phenotypes of RFP-neg cells (3831 cells) normalized to the average of scRNA-seq data for all or one of the RFP-pos clones. (i) Heatmap shows gene-dosage effects. (ii) Scatterplot shows corresponding decreased expression from Chr-5, including LMNB1 and tumor suppressor APC. (D) Average sc-RNAseg confirms downregulation of LMNB1 and APC in N3 cells, whereas Chr 6 gene HSP90AB1 shows no difference with P3; averaged from nonzero reads. (Mean and SEM; \*\*\*\*p < 0.0001; Mann-Whitney test). (E) Based on criteria from TUSON Explorer (Davoli et al., 2013), highest ranked tumor suppressor genes and oncogenes on Chr 5 were identified. APC, a tumor suppressor gene, is highly significant. Gene information: www.ncbi.nlm.nih.gov/guide/genes-expression/.



**FIGURE 3:** Loss of Chr-5 impacts mechanotypes including dissemination and proliferation. (A) P3 and N3 colonies (~20 cells, average) show noncircular clusters and isolated migratory cells (red arrowheads). The circularity C of clusters anticorrelates with the fraction of isolated cells ( $n \ge 800$  cells per condition; Mean and SEM; \*p < 0.05). B; i) Transwell migration from high density "Top" to low density "Bottom" over 24 h (*cartoon*) shows no differences in migration, but migration does lead to reentry into cell cycle (per EdU signal). (ii) N3 cells replicate and divide more than P3s ( $n \ge 1300$  cells per condition and n = 4 replicates, Mean and SEM; unpaired two-tailed t test with Welch's correction: \*p < 0.05; SEM). Scale bar = 20 μm. (C) N3 cells grow faster than P3s: (i) at low, medium, and high density for ~24 h. with EdU added in last 1 h (image). (ii) Both sparse and dense N3 cells proliferate faster. Sparse, fitted to  $y = ae^{kx}$  (for both,  $R^2 = 0.99$ ). Dense, fitted to  $y = 10^{mx+b}$  (m = 0.011 for P3, m = 0.013 for N3) and both  $R^2 = 0.99$  ( $n \ge 180$  cells per condition and n = 2 replicates; Mean and SEM; \*p < 0.05). Scale bar = 20 μm. (D) N3 Chr's show increased missegregation events during mitosis, such as micronuclei or bridge formation (N3: 3/14 cells; P3: 1/27 cells).

48

Time (h)

96

Cells/mm<sup>2</sup> 1000

10

To more thoroughly characterize any proliferative advantage of N3 cells, we assayed EdU incorporation at varying cell densities in standard 2D cultures and quantified growth curves. N3 cells show increased replication at 24 h, with decreased replication at highest density conditions, consistent with contact-inhibition (Figure 3C, i; Abercrombie, 1979). Cell counts also show that in both very sparse and denser 2D culture, N3 cells proliferate faster than P3 cells (Figure 3C, ii). The ~1.5 to two-fold higher N3 cell counts versus P3's after a few days reflects a faster doubling (27 vs. 30.5 h). Higher

48

Time (h)

Cells/mm

frequencies of mitotic missegregation events for N3 cells (Figure 3D) is consistent with APC's role in MT stabilization and mitotic fidelity (Wen et al., 2004; Caldwell and Kaplan, 2009). Faster growth and genetic instability (upon Chr mis-segregation) are two key hallmarks of cancer and consistent with deficits in APC as a tumor suppressor.

Abnormal Mitosis

To further explore the possible role of APC, we sought to disrupt APC function in P3 cells and phenocopy N3 cells (per Figure 2C, ii). The drug CHIR-99021 causes protein-level inhibition of APC and two other proteins in a key  $\beta$ -catenin destruction complex



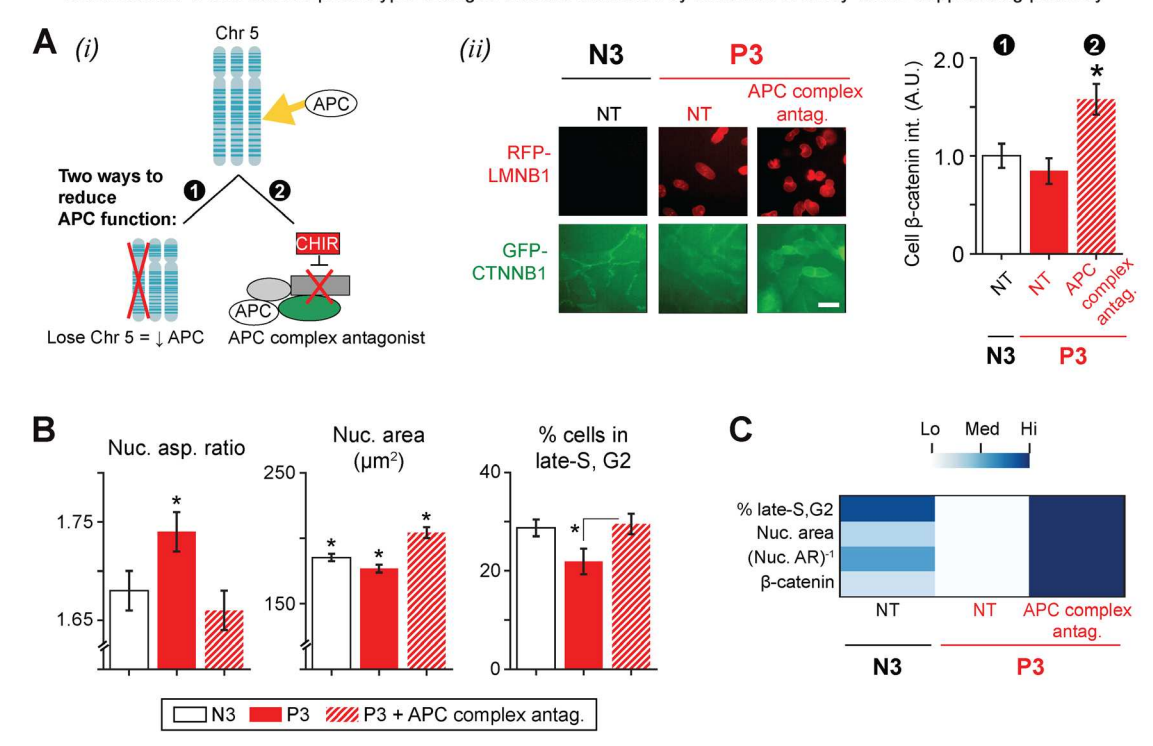


FIGURE 4: Drug inhibition of a tumor-suppressing APC pathway can phenocopy the loss of Chr5 and the APC gene. (A) Chr 5 loss could suppress APC pathways. (i) The drug CHIR-99021 inhibits a β-catenin destruction complex formed by APC and two other proteins. (ii) P3 and N3 cells were treated with the APC complex antagonist for 48 h, and β-catenin intensity was measured among cells with no neighbors ( $n \ge 9$  cells per condition; Mean and SEM; \*p < 0.05). Scale bar =  $25 \mu m$ . (B) CHIR-99021 for 24 h on P3 cells phenocopies APC loss with increased nuclear roundness, area (for DNA content), and cells in late-S/G2 phases. Mean and SEM ( $n \ge 300$  cells per condition; unpaired two-tailed t test with Welch's correction: \*p < 0.05). (C) Heat map summary.

(Figure 4A, i). P3 cells treated with the CHIR antagonist indeed show increased  $\beta$ -catenin content (~1.5-fold) when compared with nontreated cells (Figure 4A, ii). CHIR-treated P3 cells phenocopy the proliferative advantage of N3 cells relative to P3 controls while also generating distinctly larger and more rounded nuclear morphologies (Figure 4B). In general, drugs that rescue the decreased activity of Tumor Suppressor genes such as APC (in N3 cells for example) could be clinically useful but do not exist (Supplemental Table S1). APC knockdown in various cancer lines nonetheless confirm findings here for N3 cells relative to P3 cells, including mitotic aberrations (U2OS cells), more cells in S & G2M phases (MDA-MB-231 cells), and increased overall proliferation (pancreatic and lung cancer lines) (Dikovskaya et al., 2007; Lin et al., 2017; Cole et al., 2019; Astarita et al., 2021). Mechanisms seem to involve upregulation of cyclin D1 and cMyc (Heinen et al., 2002), but more rounded nuclei in APC-deficient N3 and treated P3 cells further suggest a perturbation of polarizing cytoskeletal components that could reflect diminished interaction between APC and MTs (Hernandez and Tirnauer, 2010). Thus, despite the mechano-complexity of aneuploidy (Tsai et al., 2019), a summary heat map highlights replicative and morphological differences reasonably associated with decreased APC (Figure 4C).

# **CONCLUSIONS**

Evolution involves two processes: the first is genetic variation, and the second is selection for survival of the fittest. In seeking to characterize and understand the latter in terms of mechanotype differences between genetically distinct clones, we show that a difference in Chr number between live cells is enabled by a general method of ChReporter visualization that provides confidence in genotype differences - despite evident and ongoing diversification.

The two parts of the study here compare different aneuploid A549 cells to illustrate first a confounding complexity of genotype with major mechanotypical differences (Figure 1) and then a reasonably clear genotype-mechanotype relationship (Figures 2-4). While phenotypic changes might arise from a number of diverse factors that range from intrinsically genetic to environmentallydriven epigenetic, the molecular mechanisms proposed by our genotype-mechanotype relationship is supported by drug results that implicate the main tumor suppressor gene APC on the relevant Chr. Part of Chr-5 with the APC gene is lost in a small fraction of lung cancer patients who show worse survival (Supplemental Figure S2). The latter applies to colorectal cancer (He et al., 1998; Zhang and Shay, 2017) but also other cancers (Supplemental Figure S2B, ii), consistent with a broader than appreciated role for APC as a tumor suppressor. This could be important because some types of aneuploidy, notably Chr-1 gain, drives higher LUAD patient response rates to immunotherapy (Ng et al., 2023). Regardless, the ChReporter approach seems promising for genotype-mechanotype studies of cancers, including those foundational to genetic mechano-evolution.

### **MATERIALS AND METHODS**

### Cell lines and tissue culture

The original A549 RFP-LMNB1 cell line was engineered by Sigma-Aldrich (Sigma, Catalog no. #CLL1149). A549 cells were cultured in Ham's F-12 media (Life Technologies #11765047) and supplemented with 10% fetal bovine serum (MilliporeSigma, Catalog no. #F2442) and 1% penicillin-streptomycin (Life Technologies, Catalog no. #15140122). All cells were passaged every 2–3 d using 0.05% Trypsin/ ethylenediaminetetraacetic acid (Life Technologies, Catalog no. #25300054). All cell lines were incubated at 37°C with 5% CO<sub>2</sub>.

### Cell treatments

The following chemical treatments were used: nocodazole (MilliporeSigma, Catalog no. #M1404), Latrunculin-A (MilliporeSigma, Catalog no #L5163), and GSK-3 inhibitor CHIR-99021 (MilliporeSigma, Catalog no. #SML1046).

### Immunofluorescence and imaging

Cells were fixed in 4% formaldehyde (Thermo Fisher Scientific, Catalog no. #28908) for 15 min, followed by permeabilization by 0.5% Triton-X (MilliporeSigma, Catalog no. #112298) for 15 min, and blocked with 5% bovine serum albumin (BSA; MilliporeSigma, Catalog no. #A7906) for 30 min. Nuclei were stained with 8 $\mu$ M Hoechst 33342 (Thermo Fisher, #Catalog no. 62249) for 15 min. When mounting is involved, Prolong Gold antifade reagent was used (Invitrogen, Catalog no. #P36930). Epifluorescence imaging was performed using an Olympus IX71 with a digital camera (Photometrics) and either a 10×/0.2 NA or 40×/0.6 NA objective. For certain samples, confocal imaging was performed on a Leica TCS SP8 system with a 63×/1.4 NA oil-immersion. Live imaging was performed on an EVOS FL Auto Imaging System with 10 × or 20×/0.6 NA object in normal culture conditions (37°C and 5% CO<sub>2</sub>; complete culture medium as specified above).

# Live-cell imaging of cell motility

All studied A549 RFP-LMNB1 clones were plated 24 h before assay at a density of 4000 cells per well in a 12-well plate (Corning). Live-imaging was done using an EVOS FL Auto Imaging System with a 10× objective with cells under normal culture conditions (37°C and 5%  $\rm CO_2$ ; complete culture medium). One image was taken every hour for a total of 6 h. Migration paths of cells were traced with MATLAB, with the original location of cells labeled as the origin coordinate (x, y) = (0, 0). Speed was calculated using the ImageJ Plugin MTrackJ: for each cell, its x, y coordinates were recorded by MTrackJ from t = 0 to 6 h at 1-h intervals. The mean speed |y| for each cell over the 6-h span was calculated as the sum of all distances traveled divided by total time span. Mathematically, the

expression is:  $|\mathbf{v}| = \left(\sum_{i=1}^6 \sqrt{(x_i - x_{i-1})^2 + (y_i - y_{i-1})^2}\right)/6$ , where i denotes the time step for each cell imaged. Migratory persistence P for each clone or condition was calculated as  $P = \underline{D}/|\mathbf{v}|$ , where D is the diffusion coefficient, given by the slope of the mean squared displacement (for all cells of the given clone or condition) versus time t.

# EdU labeling and staining

10  $\mu$ M 5-ethynyl-2'-deoxyuridine (EdU; Abcam, Catalog no. #ab146186) was added to 2D culture or both sides of a pore filter 1 h before fixation and permeabilization. After permeabilization, EdU-labeled cells were stained as follows by a click chemistry reaction: cells were incubated in 100 mM Tris (pH 8.5, Fisher Scientific, 77-86-1), 4 mM CuSO<sub>4</sub> (MilliporeSigma, Catalog no. #C1297), 5  $\mu$ M sulfonated Cy5 azide (Click Chemistry Tools, Catalog no. 1509), and 50 mM ascorbic acid (MilliporeSigma, Catalog no. #A8960) for 30 min, and then washed 3× with 0.1% BSA in phosphate-buffered saline.

### Transwell migration

Cells were seeded at  $4.5 \times 10^5$  cells/cm² on top of 8-µm pore filters, mounted in 24-well polycarbonate inserts (Corning). For 24 h, cells were allowed to migrate through the pores in normal culture conditions; during the last 1 h, EdU was added to the culture medium above and below each pore membrane. After the 24-h migration period, cells attached to the top and bottom of the membranes were fixed, permeabilized, and stained as described above. All membranes were mounted between glass coverslips using ProLong Gold antifade mountant. All fixation and staining steps were carried out at room temperature.

# Cell growth curves

At t=0 h, RFP-positive and RFP-negative clones (P3 and N3, respectively) were each seeded in a 24-well plate at extremely low density  $(2.6\times10^2\,\text{cells/cm}^2)$ . Starting at t=24 h, every 24 h for 96 h total, tile scanning was used to image one-half of each sample well. Imaging was performed on an Olympus IX71—with a  $10\times/0.2\,\text{NA}$  objective—and a digital EMCCD camera. For every timepoint under sparse conditions, the number of cells in each half-well was manually counted from the images, and then multiplied by two to get the total number of cells per well, or the total population of each experimental condition. For denser plating experiments, duplicate wells were trypsinized and counted. Fits to exponential growth  $y=ae^{kx}$  exclude t=0 h, where cell density is merely an estimate, and fits to  $y=10^{mx+b}$  exclude t=0 h.

### Identifying and analyzing cell clusters

Cell cluster analysis was performed using growth curve images of P3 and N3 cells at t=72 h. From both the P3 and the N3 image set, clusters comprising 10 or more cells were identified by eye, and 15 such clusters were randomly selected for analysis. Cells were classified as belonging to a cluster if they were part of–or within ~20  $\mu$ m of–a conspicuous locally dense cell aggregate. All other cells were considered isolated. Clusters were manually outlined in ImageJ (Schneider et al., 2012) to measure cluster perimeter P and area A; the latter was divided by the number of cells in the cluster to obtain area-per-cell. By contrast, average cell area was obtained by manual segmentation of individual cells. Compactness C of each cluster was calculated as  $C = 4\pi A V P^2$ , as described in (Li et al., 2013).

# scRNA-seq and analysis

RNA libraries were constructed using the Chromium Single Cell Gene Expression kit (v3.1, single index, Catalog no. #PN-1000128; #PN-1000127; #PN-1000213) from 10× Genomics per the manufacturer's instructions. Libraries were submitted to the University of Pennsylvania's Next Generation Sequencing Core for sequencing using NovaSeq 6000 (100 cycles) from Illumina. CellRanger (version 5.0.1) was used to analyze raw base call (BCL) to generate FASTQ files and the "count" command was used to generate raw count matrices aligned to GRCh38 provided by 10× genomics. The data generated was imported as a Seurat object (4.0.0) for future downstream analysis (Stuart et al., 2019; Hao et al., 2021). Cells were filtered to express between 500 and 6000 genes to eliminate low quality cells and had less than 10% mitochondrial RNA. Differential gene expression analysis was performed using the "FindAllMarkers" function and genes with nonzero expression in at least 25% of the cells in both cohorts were kept. The UMAP was created using the first 12 principle components based on the Elbow Plot. The function "AverageExpression" was used to evaluate average gene expression in each cohort and when necessary, data was normalized using the "LogNormalize" method. The biomaRT

library and useEnsembl were used to identify Chr number and hanc symbol for the genes. DAVID (Sherman et al., 2022) was used for gene annotation analysis. All sc-mRNAseg analysis was done in R version 4.0.4.

### Identification of CNV from single-cell RNAseq data

inferCNV (Tickle, 2019) was used to tag the sc-mRNAseg from A549 cells with labels of clone (P1, P2, P3, P4, N3) with annotation input being given for RFP-Pos vs RFP-Neg cells.

### Single Cell DNA-seq CNV analysis

DNA library was constructed using Chromium Single Cell DNA Reagent kits (PN-1000041, PN-1000057, PN-120262, PN-1000032, PN-1000036) from 10× Genomics (Pleasanton, CA) per the manufacturer's instructions. Library prepared was processed at the Next Generation Sequencing Core at the University of Pennsylvania (12-160, Translational Research Center, University of Pennsylvania) using NovaSeq 6000, 200 cycles (Illumina, San Diego, CA). For each sample, the copy number data was generated using Cell Ranger DNA pipeline (10x Genomics) and then exported to R to generate the copy number heatmap using "ComplexHeatmap" (2.11.1).

# TCGA LUAD patient CNV profiling and survival analyses

CNV (masked cnv) was downloaded from UCSC Xena website (https://xenabrowser.net/datapages/; Goldman et al., 2020). The CNV profile heatmap was then generated using R package "ComplexHeatmap" (v2.11.1). Patient survival curves derive from the human protein atlas, specifically using the 'pathology' tab (https:// www.proteinatlas.org/; Uhlen et al., 2015).

### TCGA and CCLE analysis

For TCGA analysis, CNV (masked cnv) and phenotype data was downloaded from UCSC Xena website (https://xenabrowser.net/ datapages/; Goldman et al., 2020). Aneuploidy level from TCGA was assessed using a recently published dataset (Knijnenburg et al., 2018). For CCLE, CNV (CCLE\_segment\_cn) and phenotype data was downloaded from the DepMap portal (https://depmap.org/ portal/download/all/).

CCLE copy number was reported as the ratio between the copy number and the basal reference of the sample, a region with two copies of Chrs will have a ratio of one. The aneuploidy level was obtained by summing |reported ratio - 1| × segment length of the reported ratio within each sample. All aneuploidy levels were normalized to the maximum.

# Reporter validation via single-nucleotide polymorphism arrays and analysis

Genomic DNA was isolated from a minimum of  $3.0 \times 10^5$  cells with the Blood & Cell Culture DNA Mini Kit (Qiagen, Catalog no. #13323) per the manufacturer's instructions. In the event that cells were very rare (such as reporter-negative cells), genomic DNA was amplified postextraction using the Illustra Single Cell GenomiPhi DNA Amplification Kit (GE Healthcare Biosciences, Catalog no. #29108107) following the manufacturer's instructions. All DNA samples were sent to The Center for Applied Genomics Core in The Children's Hospital of Philadelphia, PA, for SNP array HumanOmniExpress-24 Bead-Chip Kit (Illumina). For this array, >700,000 probes have an average inter-probe distance of ~4 kb along the entire genome. For each sample, the Genomics Core provided the data in the form of GenomeStudio files (Illumina). Chr copy number and loss of heterozygosity (LOH) regions were analyzed in GenomeStudio by using the cnvPartition plug-in (Illumina). Regions with one Chr copy number

are not associated with LOH by Illumina's algorithm. Hence, regions with one Chr copy number as given by the GenomeStudio are added to the LOH region lists. SNP array experiments also provide genotype data, which was used to give Single Nucleotide Variation (SNV) data. To increase the confidence of LOH data given by the GenomeStudio, the changes in LOH of each Chr from each sample were cross referenced to their corresponding SNV data. After extracting data from GenomeStudio, all data analysis was done in MATLAB.

### Karyotyping

Cells used for karyotyping were plated in T25 flasks (Corning), cultured for 2-3 d to reach ~50% confluency. The media was then discarded and replaced with fresh media to fill the entire flask with a closed lid, after which the flask was wrapped with parafilm. The samples were then sent to Cell Characterization Services for metaphase-spread karyotyping.

### Scaling of migratory persistence and speed

From the two-phase model of cell migration developed by Li and Sun (2018), we have the following Equation (1) for the velocity  $v_0$  of a cell migrating on a 2D substrate:

$$v_0 = \frac{L\eta J_{actin} + f_{ext}^f - f_{ext}^r}{L\eta\Theta + 2\xi L/w}$$

where L and w are the length and width of the cell, respectively;  $\eta$  is the coefficient of drag due to focal adhesions; Jactin is the rate of F-actin polymerization;  $f_{\text{ext}}^{f/r}$  is the external force per unit area at the front/rear of the cell;  $\Theta$  is the average volume fraction of the actin network; and  $\xi$  is the coefficient of friction of the substrate. In the limit of large  $\eta$  – as can be assumed for cells cultured on rigid plastic (Pelham and Wang, 1997) and especially for cells with disrupted MTs (Bershadsky et al., 1996; Enomoto, 1996) - Eq. (1) reduces to Equation (2):

$$v_0 \approx J_{actin} / \Theta$$

That is, cell velocity depends on actin polymerization rate. In turn, actin polymerization rate depends on MT activity. In two separate experiments, Waterman and coworkers measured MT growth and level of active Rac1 for 30-60 min after nocodazole washout (Waterman-Storer et al., 1999). By matching time points between these two experiments, we plotted Rac1 as a function of MT growth (Supplemental Figure S3A, i). To note, MT growth at t =30 min was not published by Waterman et al. (1999). We estimated this value by fitting power laws to the measurements of MT growth at t = 2 min and t = 20 min (with 10% of t = 2 min growth assumed at t = 0), and then extrapolating to longer times. This gives two scaling exponents-0.38 and 0.60-for the two metrics of MT growth used by Waterman et al. (1999); thus, we estimate that active Rac1 level goes like MT growth to the power of 1/2, or [GTP-Rac1] ~[MT]<sup>0.5</sup>. Assuming a linear relationship between [GTP-Rac1] and F-actin polymerization rate, as in the mechanochemical coupling model of cell polarization developed by Copos and Mogilner (2020), we obtain Equation (3):

$$v_0 \sim J_{actin} / \Theta \sim [MT]^{0.5}$$

MTs are critical for maintaining front-rear cell polarization and are therefore expected to promote migratory persistence P. Pegtel and colleagues (2007) measured the persistence of migrating cells treated with different doses of nocodazole. In replotting their data,

we find that persistence is inversely proportional to nocodazole concentration (Supplemental Figure S3A, ii). Across the range of nocodazole concentrations in Supplemental Figure S3A, iii), the relationship between MT activity and [noco.] is assumed to be in a linear regime. This assumption is based on an experiment performed by Vasquez and coworkers (1997), whereby two different cell types were treated with different doses of nocodazole, and then measured for such parameters as MT elongation velocity, catastrophe frequency, and dynamicity. MT dynamicity, an estimate of the number of tubulin subunits exchanged at MT ends, is plotted in Supplemental Figure S3A, iii) as a function of [noco.]. Because P is inversely proportional to nocodazole concentration, which varies linearly with [MT], it follows that  $P \sim$  [MT]. Finally, because  $v_0 \sim [MT]^{0.5}$  and  $P \sim [MT]$ , we predict that  $P \sim v_0^2$ , which is indeed the scaling relationship observed between migratory persistence and speed.

# Statistics and reproducibility

The statistical methods for each experiment are included in the corresponding Figure legends. Significance was determined by an unpaired student's t test unless otherwise noted. All statistical analyses were done using Python, R (version 4.0.4), and GraphPad Prism 9.0.

### **ACKNOWLEDGMENTS**

This work was supported by funding from the National Institutes of Health/National Cancer Institute (U01CA254886; P01 CA265794) and grants from National Science Foundation (MRSEC DMR-1720530 and DMR-1420530; and Grant Agreements CMMI 1548571 and 154857) and Pennsylvania Department of Health Grant Harm Reduction Futures Fund 4100083101. M.P.T. is supported by Graduate Research Fellowships from the National Science Foundation (DGE-1845298). The content of this article is solely the responsibility of the authors and does not necessarily represent the official views of the National Institutes of Health or the National Science Foundation. The results published here are in part based upon data generated by The Cancer Genome Atlas (TCGA) Research Network: www .cancer.gov/tcga. We gratefully acknowledge the following core facilities across the University of Pennsylvania Perelman School of Medicine for instrument access and assistance: Flow Cytometry and Cell Sorting Core, Next Generation Sequencing Core, and the Cell & Developmental Biology Microscopy Core. We also thank The Center for Applied Genomics Core in The Children's Hospital of Philadelphia for all SNPa analyses and support.

### **REFERENCES**

- Abercrombie M (1979). Contact inhibition and malignancy. Nature 281, 259–262.
- Astarita EM, Maloney SM, Hoover CA, Berkeley BJ, VanKlompenberg MK, Nair TM, Prosperi JR (2021). Adenomatous Polyposis Coli loss controls cell cycle regulators and response to paclitaxel in MDA-MB-157 metaplastic breast cancer cells. PLoS One 16, e0255738.
- Bershadsky A, Chausovsky A, Becker E, Lyubimova A, Geiger B (1996). Involvement of microtubules in the control of adhesion-dependent signal transduction. Curr Biol 6, 1279–1289.
- Buxboim A, Irianto J, Swift J, Athirasala A, Shin JW, Rehfeldt F, Discher DE (2017). Coordinated increase of nuclear tension and lamin-A with matrix stiffness outcompetes lamin-B receptor that favors soft tissue phenotypes. Mol Biol Cell 28, 3333–3348.
- Caldwell CM, Kaplan KB (2009). The role of APC in mitosis and in chromosome instability. Adv Exp Med Biol 656, 51–64.
- Carterson AJ, Honer zu Bentrup K, Ott CM, Clarke MS, Pierson DL, Vanderburg CR, Buchanan KL, Nickerson CA, Schurr MJ (2005). A549 lung epithelial cells grown as three-dimensional aggregates: alternative

- tissue culture model for Pseudomonas aeruginosa pathogenesis. Infect Immun 73, 1129–1140.
- Chang YC, Nalbant P, Birkenfeld J, Chang ZF, Bokoch GM (2008). GEF-H1 couples nocodazole-induced microtubule disassembly to cell contractility via RhoA. Mol Biol Cell 19, 2147–2153.
- Cole JM, Simmons K, Prosperi JR (2019). Effect of adenomatous polyposis coli loss on tumorigenic potential in pancreatic ductal adenocarcinoma. Cells 8, 1084.
- Copos C, Mogilner A (2020). A hybrid stochastic-deterministic mechanochemical model of cell polarization. Mol Biol Cell 31, 1637–1649.
- Davoli T, Xu AW, Mengwasser KE, Sack LM, Yoon JC, Park PJ, Elledge SJ (2013). Cumulative haploinsufficiency and triplosensitivity drive aneuploidy patterns and shape the cancer genome. Cell 155, 948–962.
- De Brabander MJ, Van de Veire RM, Aerts FE, Borgers M, Janssen PA (1976). The effects of methyl (5-(2-thienylcarbonyl)-1H-benzimidazol-2-yl) carbamate, (R 17934; NSC 238159), a new synthetic antitumoral drug interfering with microtubules, on mammalian cells cultured in vitro. Cancer Res 36, 905–916.
- Dikovskaya D, Schiffmann D, Newton IP, Oakley A, Kroboth K, Sansom O, Jamieson TJ, Meniel V, Clarke A, Nathke IS (2007). Loss of APC induces polyploidy as a result of a combination of defects in mitosis and apoptosis. J Cell Biol 176, 183–195.
- Enomoto T (1996). Microtubule disruption induces the formation of actin stress fibers and focal adhesions in cultured cells: possible involvement of the rho signal cascade. Cell Struct Funct 21, 317–326.
- Faux MC, Ross JL, Meeker C, Johns T, Ji H, Simpson RJ, Layton MJ, Burgess AW (2004). Restoration of full-length adenomatous polyposis coli (APC) protein in a colon cancer cell line enhances cell adhesion. J Cell Sci 117, 427–439.
- Foster KA, Oster CG, Mayer MM, Avery ML, Audus KL (1998). Characterization of the A549 cell line as a type II pulmonary epithelial cell model for drug metabolism. Exp Cell Res 243, 359–366.
- Garay T, Juhasz E, Molnar E, Eisenbauer M, Czirok A, Dekan B, Laszlo V, Hoda MA, Dome B, Timar J, et al. (2013). Cell migration or cytokinesis and proliferation?—revisiting the "go or grow" hypothesis in cancer cells in vitro. Exp Cell Res 319, 3094–3103.
- Giard DJ, Aaronson SA, Todaro GJ, Arnstein P, Kersey JH, Dosik H, Parks WP (1973). In vitro cultivation of human tumors: establishment of cell lines derived from a series of solid tumors. J Natl Cancer Inst 51, 1417–1423.
- Giese A, Loo MA, Tran N, Haskett D, Coons SW, Berens ME (1996). Dichotomy of astrocytoma migration and proliferation. Int J Cancer 67, 275–282.
- Goldman MJ, Craft B, Hastie M, Repecka K, McDade F, Kamath A, Banerjee A, Luo Y, Rogers D, Brooks AN, et al. (2020). Visualizing and interpreting cancer genomics data via the Xena platform. Nat Biotechnol 38, 675–678.
- Hanahan D, Weinberg RA (2011). Hallmarks of cancer: the next generation. Cell 144, 646–674.
- Hankey W, Frankel WL, Groden J (2018). Functions of the APC tumor suppressor protein dependent and independent of canonical WNT signaling: implications for therapeutic targeting. Cancer Metastasis Rev 37, 159–172.
- Hao Y, Hao S, Andersen-Nissen E, Mauck WM 3rd, Zheng S, Butler A, Lee MJ, Wilk AJ, Darby C, Zager M, et al. (2021). Integrated analysis of multimodal single-cell data. Cell 184, 3573–3587 e3529.
- Hayes BH, Zhu PK, Wang M, Pfeifer CR, Xia Y, Phan S, Andrechak JC, Du J, Tobin MP, Anlas A, et al. (2023). Confinement plus Myosin-II suppression maximizes heritable loss of chromosomes, as revealed by live-cell ChReporters. J Cell Sci 136, jcs260753.
- He TC, Sparks AB, Rago C, Hermeking H, Zawel L, da Costa LT, Morin PJ, Vogelstein B, Kinzler KW (1998). Identification of c-MYC as a target of the APC pathway. Science 281, 1509–1512.
- Heinen CD, Goss KH, Cornelius JR, Babcock GF, Knudsen ES, Kowalik T, Groden J (2002). The APC tumor suppressor controls entry into S-phase through its ability to regulate the cyclin D/RB pathway. Gastroenterology 123, 751–763.
- Hernandez P, Tirnauer JS (2010). Tumor suppressor interactions with microtubules: keeping cell polarity and cell division on track. Dis Model Mech 3, 304–315.
- Holland AJ, Cleveland DW (2009). Boveri revisited: chromosomal instability, aneuploidy and tumorigenesis. Nat Rev Mol Cell Biol 10, 478–487.
- Irianto J, Xia Y, Pfeifer CR, Greenberg RA, Discher DE (2017). As a nucleus enters a small pore, chromatin stretches and maintains integrity, even with DNA breaks. Biophys J 112, 446–449.

- Knijnenburg TA, Wang L, Zimmermann MT, Chambwe N, Gao GF, Cherniack AD, Fan H, Shen H, Way GP, Greene CS, et al. (2018). Genomic and molecular landscape of DNA damage repair deficiency across The Cancer Genome Atlas. Cell Rep 23, 239-254 e236.
- Li WG, Goodchild MF, Church R (2013). An efficient measure of compactness for two-dimensional shapes and its application in regionalization problems. Int J Geo Inf Sci 27, 1227-1250.
- Lin Y, Gu Q, Sun Z, Sheng B, Qi C, Liu B, Fu T, Liu C, Zhang Y (2017). Upregulation of miR-3607 promotes lung adenocarcinoma proliferation by suppressing APC expression. Biomed Pharmacother 95, 497–503.
- Li Y, Sun SX (2018). Transition from actin-driven to water-driven cell migration depends on external hydraulic resistance. Biophys J 114, 2965–2973.
- Martincorena I, Raine KM, Gerstung M, Dawson KJ, Haase K, Van Loo P, Davies H, Stratton MR, Campbell PJ (2017). Universal patterns of selection in cancer and somatic tissues. Cell 171, 1029-1041 e1021
- Ng KW, Boumelha J, Enfield KSS, Almagro J, Cha H, Pich O, Karasaki T, Moore DA, Salgado R, Sivakumar M, et al. (2023). Antibodies against endogenous retroviruses promote lung cancer immunotherapy. Nature 616, 563-573.
- Pavelka N, Rancati G, Zhu J, Bradford WD, Saraf A, Florens L, Sanderson BW, Hattem GL, Li R (2010). Aneuploidy confers quantitative proteome changes and phenotypic variation in budding yeast. Nature 468, 321-325.
- Pegtel DM, Ellenbroek SI, Mertens AE, van der Kammen RA, de Rooij J, Collard JG (2007). The Par-Tiam1 complex controls persistent migration by stabilizing microtubule-dependent front-rear polarity. Curr Biol 17,
- Pelham RJ, Jr., Wang Y (1997). Cell locomotion and focal adhesions are regulated by substrate flexibility. Proc Natl Acad Sci USA 94, 13661-13665.
- Pfeifer CR, Xia Y, Zhu K, Liu D, Irianto J, Garcia VMM, Millan LMS, Niese B, Harding S, Deviri D, et al. (2018). Constricted migration increases DNA damage and independently represses cell cycle. Mol Biol Cell 29, 1948-1962
- Schneider CA, Rasband WS, Eliceiri KW (2012). NIH Image to ImageJ: 25 years of image analysis. Nat Methods 9, 671-675.
- Schneikert J, Behrens J (2007). The canonical Wnt signalling pathway and its APC partner in colon cancer development. Gut 56, 417-425.
- Sherman BT, Hao M, Qiu J, Jiao X, Baseler MW, Lane HC, Imamichi T, Chang W (2022). DAVID: a web server for functional enrichment analysis and functional annotation of gene lists (2021 update). Nucleic Acids Res
- Spector I, Shochet NR, Blasberger D, Kashman Y (1989). Latrunculins-novel marine macrolides that disrupt microfilament organization and affect cell

- growth: I. Comparison with cytochalasin D. Cell Motil Cytoskeleton 13,
- Stingele S, Stoehr G, Peplowska K, Cox J, Mann M, Storchova Z (2012). Global analysis of genome, transcriptome and proteome reveals the response to aneuploidy in human cells. Mol Syst Biol 8, 608
- Stuart T, Butler A, Hoffman P, Hafemeister C, Papalexi E, Mauck WM 3rd, Hao Y, Stoeckius M, Smibert P, Satija R (2019). Comprehensive integration of single-cell data. Cell 177, 1888-1902 e1821.
- Tickle T, Tirosh I, Georgescu C, Brown M, Haas B (2019). inferCNV of the Trinity CTAT Project. Klarman Cell Observatory Cambridge MA: Broad Institute of MIT and Harvard.
- Torres EM, Dephoure N, Panneerselvam A, Tucker CM, Whittaker CA, Gygi SP, Dunham MJ, Amon A (2010). Identification of aneuploidy-tolerating mutations. Cell 143, 71-83.
- Tsai HJ, Nelliat AR, Choudhury MI, Kucharavy A, Bradford WD, Cook ME, Kim J, Mair DB, Sun SX, Schatz MC, Li R (2019). Hypo-osmotic-like stress underlies general cellular defects of aneuploidy. Nature 570, 117-121.
- Uhlen M, Fagerberg L, Hallstrom BM, Lindskog C, Oksvold P, Mardinoglu A, Sivertsson A, Kampf C, Sjostedt E, Asplund A, et al. (2015). Proteomics. Tissue-based map of the human proteome. Science 347, 1260419.
- Vasquez RJ, Howell B, Yvon AM, Wadsworth P, Cassimeris L (1997). Nanomolar concentrations of nocodazole alter microtubule dynamic instability in vivo and in vitro. Mol Biol Cell 8, 973-985.
- Wang M, Phan S, Hayes BH, Discher DE (2023). Genetic heterogeneity in p53-null leukemia increases transiently with spindle assembly checkpoint inhibition and is not rescued by p53. Chromosoma, https://doi.org/ 10.1002/tea.21221.
- Waterman-Storer CM, Worthylake RA, Liu BP, Burridge K, Salmon ED (1999). Microtubule growth activates Rac1 to promote lamellipodial protrusion in fibroblasts. Nat Cell Biol 1, 45-50.
- Wen Y, Eng CH, Schmoranzer J, Cabrera-Poch N, Morris EJ, Chen M, Wallar BJ, Alberts AS, Gundersen GG (2004). EB1 and APC bind to mDia to stabilize microtubules downstream of Rho and promote cell migration. Nat Cell Biol 6, 820-830.
- Xia Y, Ivanovska IL, Zhu K, Smith L, Irianto J, Pfeifer CR, Alvey CM, Ji J, Liu D, Cho S, et al. (2018). Nuclear rupture at sites of high curvature compromises retention of DNA repair factors. J Cell Biol 217, 3796-3808.
- Zhang L, Shay JW (2017). Multiple roles of APC and its therapeutic implications in colorectal cancer. J Natl Cancer Inst 109, djw332.
- Zheng PP, Severijnen LA, van der Weiden M, Willemsen R, Kros JM (2009). Cell proliferation and migration are mutually exclusive cellular phenomena in vivo: implications for cancer therapeutic strategies. Cell Cycle 8,